Journal of Colloid and Interface Science 584 (2021) 729–737

Contents lists available at ScienceDirect

Journal of Colloid and Interface Science

journal homepage: www.elsevier.com/locate/jcis

Regular Article

Synthesis of raspberry-like antimony-platinum (SbPt) nanoparticles as highly active electrocatalysts for hydrogen evolution reaction

Cheng-Ying Chan, Chao-Hung Chang, Hsing-Yu Tuan *

Department of Chemical Engineering, National Tsing Hua University, 101, Section 2, Kuang-Fu Road, Hsinchu 30013, Taiwan

GRAPHICAL ABSTRACT

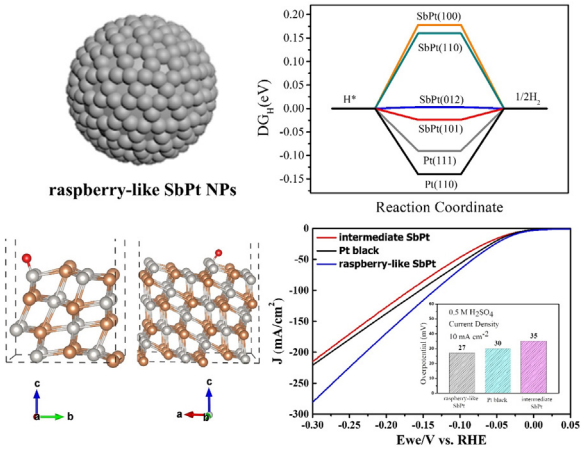

ARTICLE INFO

Article history:
Received 9 July 2020
Revised 23 September 2020
Accepted 24 September 2020
Available online 6 October 2020

Keywords:
Colloidal synthesis
Hydrogen evolution reaction
Electrocatalysis
DFT simulation
Nanoparticles
Pt-based material

ABSTRACT

Binary transition metals can facilitate the hydrogen evolution reaction (HER) through the synergistic integration of different electrochemical properties. To determine binary transition metals that are highly active, Greely et al. conducted a simulation of 256 different binary transition metals. They demonstrated that BiPt, PtRu, AsPt, SbPt, BiRh, RhRe, PtRe, AsRu, IrRu, RhRu, IrRe, and PtRh could be used as efficient electrocatalysts for HER. However, only few of them are synthesized and used as electrocatalysts. In this work, we report the synthesis of the raspberry-like antimony–platinum (SbPt) nanoparticles (NPs) *via* a colloidal nanocrystal synthesis. These NPs exhibited efficient activity with a low overpotential of 27 mV to reach 10 mA cm^{-2} in acidic media. We conducted long-term durability test for 90,000 s under an applied voltage of 0.5 V (*vs.* RHE) and cycling tests of over 10,000 cycles under an applied voltage of 0.1 to −0.5 V (*vs.* RHE). The high activity exhibited by the raspberry-like SbPt NPs may be due to the following reasons: (1) the raspberry-like SbPt NPs exhibited versatile active exposed (110), (100), (101), and (012) facets as efficient HER catalysts, and (2) as confirmed by both the density functional theory (DFT) simulation and experimental results, the presence of Sb 3d subsurface broadened the Pt surface d-band, which caused synergistic effects on water splitting. In summary, synthesis of the new colloidal

* Corresponding author.
E-mail address: hytuan@che.nthu.edu.tw (H.-Y. Tuan).

https://doi.org/10.1016/j.jcis.2020.09.099

raspberry-like SbPt NPs is essential to elucidate the fundamental properties of the nanomaterial and nanostructure design. This study could facilitate the development of Pt-group materials that can be used as HER catalysts.

1. Introduction

Hydrogen (H_2), which is a sustainable, clean, and high-energy density energy resource, has been considered as a promising candidate for resolving ecological crisis [1]. To induce the electrolysis reaction with low overpotential, the use of an efficient electrocatalyst is required. Among all electrocatalysts, which include sulfides, phosphides, carbides, borides, nitrides, and metal-free materials, Pt and Pt-group materials are still considered as the most active electrocatalysts for HER owing to their ability to easily initiate proton reduction pathway in a relatively small overpotential. Moreover, they exhibit efficient catalytic performance with high exchange current densities [2,3]. However, their wide application may be hindered by the scarcity of the Pt element [4,5].

With the aim of mitigating the use of Pt, great effort has been exerted to develop Pt structures and incorporate other metals into Pt-forming alloys, such as FePt, NiPt, SnPt, $GaPt_3$, $CoPt_3$, MnPt, GePt, PdPt, VPt_3, $CuPt_3$, and ZnPt [6–16]. In the theory of HER, the free energy of H_2 adsorption on the surface is critically treated as the descriptor for the quantification of the efficiency of the catalysts. Greely et al. conducted a surface simulation of 256 different binary transition metals to determine the strong synthetic catalysts, including BiPt, PtRu, AsPt, SbPt, BiRh, RhRe, PtRe, AsRu, IrRu, RhRu, IrRe, and PtRh [17]. However, only a few of them have been reported as water splitting electrocatalysts, including BiPt [18] and PtRu [19,20]. The presence of Sb 3d subsurface has been proven to broaden the Pt surface d-band, with synergistic effects on electronic modifications and chemical property, which results in the weakening of the adsorption energies between surfaces with H_2 or oxygen [21–23].

In electrochemistry, elemental Sb NPs have been used, including Li-ion and Na-ion batteries [24], as well as conductive antimony tin oxide (ATO) [25]. The SbPt intermetallic compounds have five intermetallic phases: $SbPt_7$, $SbPt_3$, Sb_2Pt_3, SbPt, and Sb_2Pt [26]. SbPt synthesis was performed *via* arc melting and sintering, procedures which are applied in methanol electro-oxidation [27]. SbPt/C can also function as a selective electro-oxidation catalyst for transforming glycerol to dihydroxyacetone [28]. The existence of Sb exerts predictable geometric structural and synergistic effects: increased enthalpy could be attributed to higher chemical and structural stability and thus to make SbPt a durable electrocatalyst. However, studies on the synthesis of nanosized SbPt used in electrolysis are poorly understood.

In this work, we conduct synthesis of colloidal SbPt NPs used in HER through the decomposition of Pt(II) iodide and Sb(III) iodide coated with oleylamine. At the start of the nucleation, intermediate SbPt NPs formed. After being left to stand at a temperature of 150 °C for 20 min, the raspberry-like SbPt NPs formed as the final products. These NPs exerted a synergistic effect on the HER activity, which resulted in a higher activity (27 mV to achieve 10 mA cm^{-2}) compared with Pt (30 mV) in acidic media. Moreover, the raspberry-like SbPt NPs exhibited excellent durability for 90,000 s under an applied voltage of 0.5 V (*vs.* RHE) and remained activity after 10,000 CV cycles. The calculated electrochemically active surface area (ECSA) value of the as-prepared raspberry-like SbPt NPs is 33.6 m^2 g^{-1}, which is 1.25 times larger than that of Pt black. The DFT simulation revealed that the presence of Sb is important for the electronic and synergistic effects and thus for enhancing HER activity. The DFT simulation of the raspberry-like SbPt NPs with observed exposed (110), (100), (101), and (012) facets could facilitate HER; moreover, the Gibbs free energy of H_2 adsorption (ΔG_{H^*}) of (101) and (012) of the raspberry-like SbPt NPs is closer to zero than that of Pt black.

2. Experimental details

2.1. Materials and reagents

Chemicals purchased from Sigma-Aldrich: antimony (III) iodide (SbI_3, 98%, CAS-NO. 7790–44-5), oleylamine (OLA, 70%, CAS-NO.112–90-3), toluene (>99.5%), sulfuric acid (ACS reagent grade, 95–98%), and ethanol (>99.5%, absolute). Others listed below procured from Alfa Aesar: platinum (II) iodide (PtI_2, 98%, CAS-NO. 7790-39-8), hexamethyldisilazane (HMDS, 98%, CAS-NO. 999-97-3), and 1-octadecene (1-ODE, technical grade, 90%, CAS-NO. 112-88-9). All chemicals were applied as received.

2.2. Synthesis of intermediate and raspberry-like SbPt nanoparticles

In a typical synthesis, 4 mL of yellow-light stock solution containing oleylamine (OLA) and PtI_2 (46.4 mg) was added to a well-dispersed transparent solution composed of 5 mL of OLA, 5 mL of 1-octadecene and SbI_3 (48 mg) in three-neck flask under argon environment. Then, 1 mL of hexamethyldisilazane (HMDS) was injected. The mixture solution was heated to 150 °C at a rate of 2 °C min^{-1}. At the beginning of nucleation, after the solution was kept at 150 °C for about 8 min, it formed intermediate SbPt nanoparticles. After further kept at 150 °C for 20 min. it formed stable raspberry-like SbPt nanoparticles. The reaction was quenched by water bath and the solution is divided into two tubes. Toluene is added until 45 mL per tube and followed by centrifugation two times with the ration of toluene and ethanol 1: 1.5 at 8000 rpm for 5 min with the solid parts remained, which were our product raspberry-like SbPt nanoparticles, kept in vacuum environment.

2.3. Characterization techniques

The morphologies of SbPt nanoparticles were acquired by scanning electron microscopy (SEM) (Hitachi SU8010) equipped with energy-dispersive X-ray spectroscopy (EDS) detector. Transmission electron microscopy (TEM) (JEOL, JEM-ARM200FTH, services provided by NTHU and NCTU) with an accelerating voltage of 200 kV for investigating further structure analysis including morphology, HRTEM, and SAED. The X-ray photoelectron spectroscopy (XPS) characteristic peaks were conducted with ULVAC-PHI Quantera II. All the spectra obtained from XPS analysis were first calibrated by referencing binding energy of C 1s (284.8 eV), followed by the curve fitting using the software of XPSPEAK VER. 4.1. The X-ray diffractometer (XRD, D8 advance eco (Bruker)) data were obtained with Cu radiation source (λ = 1.54 Å).

2.4. Electrochemical measurements

All electrochemical data were recorded in a typical three-electrode system connected with an electrochemical workstation (Bio-Logic-science Instruments, VMP3) at room temperature. All

reported potentials in this study were adjusted to the reversible hydrogen electrode (RHE) as reference with no IR compensation in an 0.5 M H_2SO_4 electrolyte, a platinum wire as the counter electrode. The working electrode was prepared as following content: add 6 mg of SbPt powders in a 7 mL sample vial with 2 mL of toluene and sonicated for about one hour. Then, 5 μL of the obtained solution was immediately deposited onto the rotation disk electrode (glassy carbon, D = 0.5 cm, Area = 0.196 cm^2) two times at room temperature.

All the HER measurements were conducted in 0.5 M H_2SO_4, the linear sweep voltammetry (LSV) was measured at a scan rate of 5 mV s^{-1} in the range from 0.2 V to − 0.5 V (*vs.* RHE), and the long-term durability test data was measured at a current density of 50 mA cm^{-2} for 90,000 s under the electrode rotation rate 3000 rpm. Cyclic voltammetry (CV) was performed from 0.2 V to −0.5 V (*vs.* RHE) at the speed of 100 mV s^{-1} for 10,000 cycles. Electric impedance spectroscopy (EIS) measurements were carried out at a frequency ranging from 10^5 to 0.01 Hz with a voltage −0.12 V (*vs.* RHE).

3. Result and discussion

We referred to the phase diagram of Sb and Pt (Fig. S1) to determine the stable temperature and concentration intervals of the SbPt alloys [26]. SbPt NPs were synthesized *via* a colloidal reaction, as presented in the schematic diagram in Fig. 1. Basically, SbI_3 and PtI_2 as precursors were placed in a three-neck flask; then 1-ODE and OLA as the capping agent and solvent, respectively, were added. Subsequently, the reaction was induced by heating at a temperature of 150 °C to allow the formation of intermediate SbPt NPs. Then, after being left to stand at 150 °C for 20 min, the raspberry-like SbPt NPs formed *via* the nanoscopic self-assembly process, which was driven by temperature. In this reaction, iodide

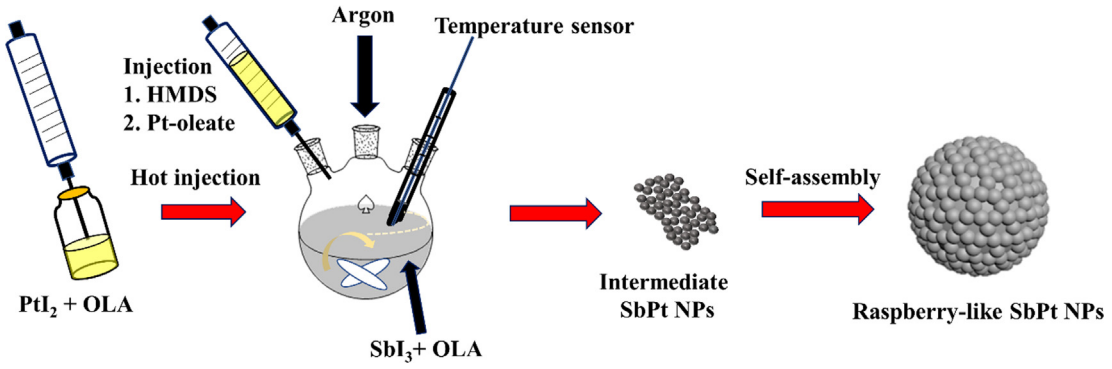

Fig. 1. Schematic diagram of colloidal synthesis of intermediate SbPt nanoparticles and raspberry-like SbPt nanoparticles.

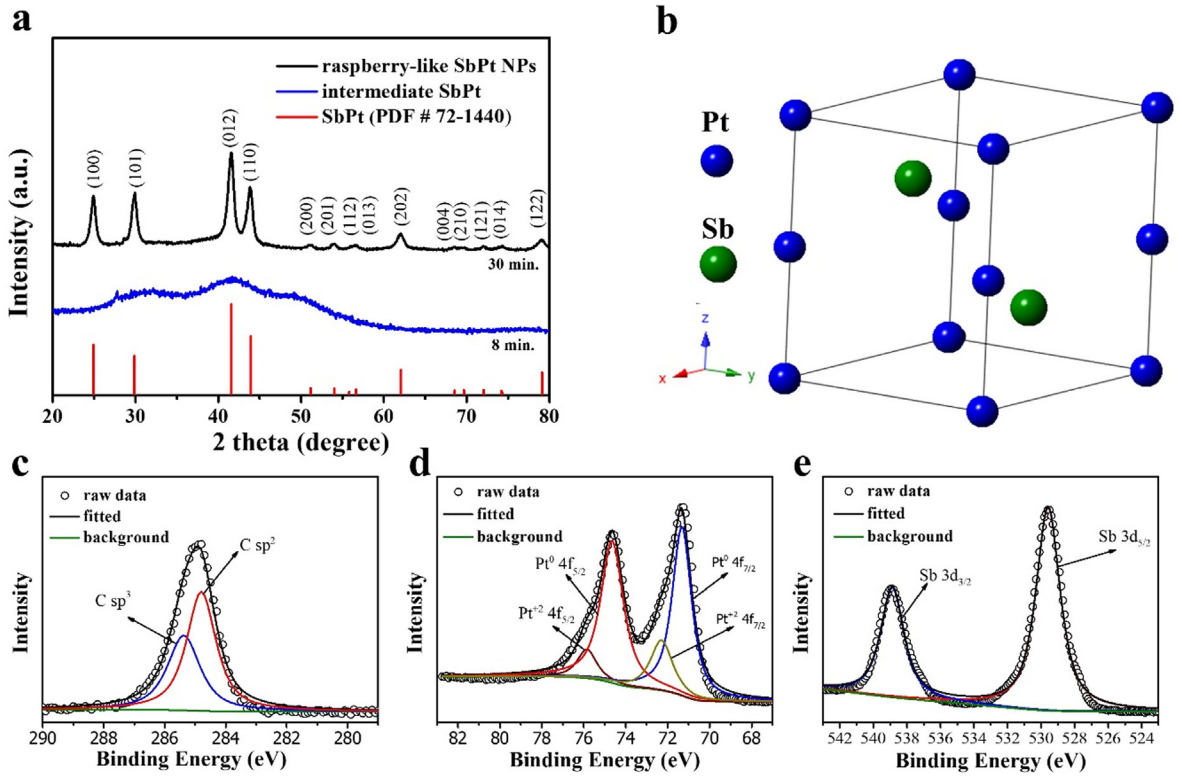

Fig. 2. The raspberry-like SbPt NPs (a) XRD pattern of raspberry-like SbPt NPs and intermediate SbPt along with the corresponding XRD database. (PDF No. 72-1440) (b) The simulated unit cell of hexagonal raspberry-like SbPt NPs. (c–e) XPS analysis of (c) Pt: 4f, (d) Sb: 3d and (e) C: 1s.

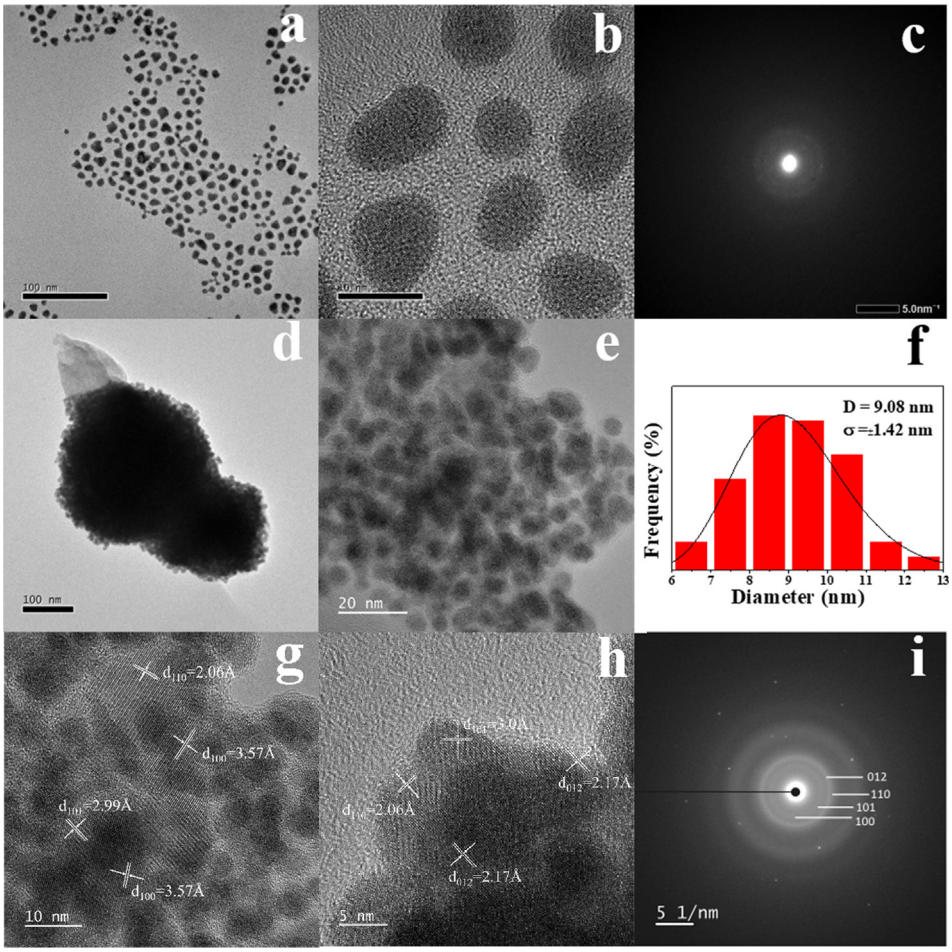

Fig. 3. (a–c) Intermediate SbPt nanoparticles (a) low magnification TEM images. (b) High magnification TEM images. (c) SAED pattern; (d–i) Raspberry-like SbPt nanoparticles. (d) Low magnification TEM images. (e) High magnification TEM images. (f) Statistics of the SbPt microsphere diameter. (g–h) HRTEM images. (i) Corresponding indexed SAED pattern.

compounds were selected as the precursors owing to their ability to completely decompose at a lower temperature.

In Fig. 2(a), the X-ray diffraction (XRD) patterns of the raspberry-like SbPt NPs exhibited 14 major characteristic peaks: 24.94°, 29.87°, 41.57°, 43.92°, 51.16°, 54.02°, 55.83°, 56.65°, 62.07°, 68.57°, 69.67°, 72.07°, 74.21°, and 79.12°, which can be indexed to (100), (101), (012), (110), (200), (201), (112), (013), (202), (004), (210), (121), (014), and (122), respectively. The high-intensity XRD spectrum demonstrated no impurity or merely little purity following the synthesis. The XRD characteristic peaks matched well with those of the hexagonal SbPt crystal (PDF No. 72-1440) [29]. Fig. 2(b) presents the simulated raspberry-like SbPt NP unit cell with a hexagonal structure in the space group $P6_3/m$ with a lattice parameter (a = b = 4.13, c = 5.47). X-ray photoelectron spectroscopy (XPS) analyses of the raspberry-like SbPt NPs were conducted to determine the elemental composition and surface electronic state [30]. Calibration of all the binding energies was performed, with reference to the C 1s peak of adventitious carbon (284.8 eV). The survey on the XPS spectra is demonstrated in Fig. 2(c–e), where three characteristic peaks were detected, referring to Pt 4f, Sb 3d, and C 1s; the full spectra of SbPt are also provided in Fig. S2. As presented in Fig. 2(c–e), the center of C 1s is 248.8 eV, and by observing the C 1s peak, a small upshift tail was found. The C 1s peak was combined with two peaks of sp^2 orbit at 284.8 eV and slight sp^3 orbit at 285.4 eV. High-intensity Sb prominent peaks were obtained at 538.9 and 529.5 eV, corresponding to $3d_{3/2}$ and $3d_{5/2}$ respectively, which can be attributed to metallic Sb^0 [31,32]. This indicated that the precursors were efficiently reduced during the synthesis. The Pt spectrum of SbPt can be deconvoluted into Pt^0 ($4f_{7/2}$ 71.35 eV, $4f_{5/2}$ 74.75 eV) and Pt^{2+} ($4f_{7/2}$ 72.35 eV, $4f_{5/2}$ 75.85 eV) [33]. More importantly, the slight positive shifts within the binding energies of Pt 4f compared with bulk Pt (70.90 and 74.25 eV) indicated that Pt bonded with the Sb metal [34].

The morphology of intermediate SbPt nanocrystals was presented in low/high magnification (Fig. 3(a and b)). Weak crystal signals were detected using the selected area electron diffraction (SAED) pattern (Fig. 3(c)). The morphology of the raspberry-like SbPt NPs is presented in Fig. 3(d and e). Moreover, the average diameters of colloidal SbPt NPs were 9.08 ± 1.42 nm, as presented in the histogram (Fig. 3(f)); after the initiation of the self-assembly process, a raspberry-like structure was generated, with sizes ranging from 150 to 250 nm. The high-resolution transmission electron microscopy images of the raspberry-like SbPt NPs with different surface areas, as presented in Fig. 3(g–h), matched the XRD results. Moreover, the lattice d-space of the as-synthesized raspberry-like SbPt NPs were 3, 3.5, and 2.17 Å, which correspond to (101), (100), and (012), respectively. In Fig. 3(i), the SAED pattern of the raspberry-like SbPt NPs represents the polycrystalline structure consistent with the (110), (100), (101), and (012) crystal planes. The growth mechanism of the nanostructures from intermediate NPs to raspberry-like SbPt NPs is described below

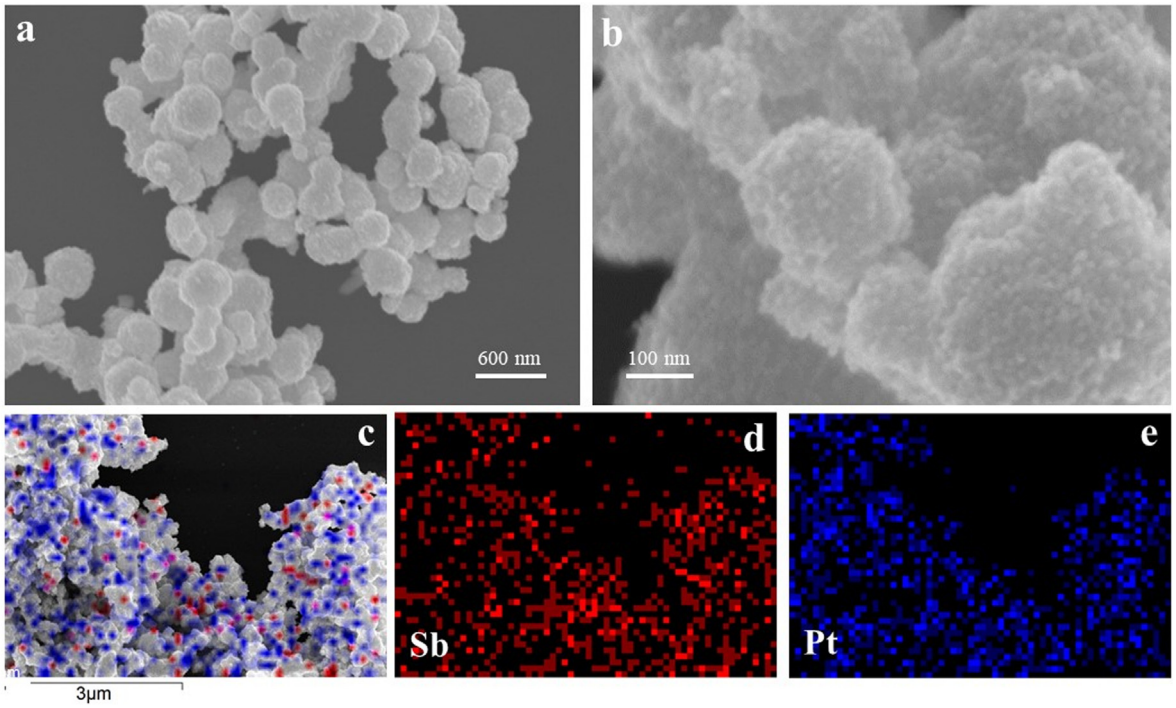

Fig. 4. The raspberry-like SbPt nanoparticles. (a-b) Low/high magnification SEM image. (c) Elemental mapping image of the raspberry-like SbPt nanoparticles. (d–e) The corresponding element Sb (red) and Pt (blue). (Data obtained by the emission of Sb Lα and Pt Mα.) (For interpretation of the references to colour in this figure legend, the reader is referred to the web version of this article.)

[35–37]. At the start of the synthesis, the reactants usually form intermediate/quasi NPs, and when the contraction of NPs reach a critical value, they further self-assemble to a stable formation, thus generating the raspberry-like structure. The formation of the raspberry-like structure could enhance the electrocatalytic performance of the nanomaterial and provide higher surface area with more available active sites during the electrochemical reaction [35]. The higher activity exhibited by the raspberry-like structure may be due to the increase in roughness. In previous reports, a similar overall behavior was observed in the raspberry-like gold microspheres, which were found to exhibit better electrochemical performance owing to their high active surface area [36]. The uneven surface of the raspberry-like structure could provide extensive active sites and further contribute to the enhancement of the catalytic performance. Altogether, the XRD and XPS measurements suggested the synthesis of SbPt without any impurities. Moreover, the SEM images (Figs. 4(a and b) and S3) show a raspberry-like structure, and the elemental composition is further presented in the SEM mapping image (Fig. 4(c)) with the corresponding elemental emission of Sb Lα (red) and Pt Mα (blue) (Fig. 4(d and e)). The energy-dispersive spectroscopy mapping is also presented in Fig. S4.

The electrocatalytic activity of the as-synthesized raspberry-like SbPt NPs sin acidic HER was investigated *via* linear sweep voltammetry (LSV). Fig. 5(a) presents the overlay of LSV curves. Compared with Pt black and intermediate SbPt, the raspberry-like SbPt NPs exhibit an extraordinary activity of only 27 mV to achieve 10 mA cm^{-2}, with no IR correction in acidic media (0.5 M H_2SO_4). Conversely, Pt and intermediate SbPt require 30 and 35 mV to reach 10 mA cm^{-2}, whereas Pt-group materials usually require 20–100 mV [38,39]. SbPt was compared with other Pt-group materials, as presented in Table S1. As can be seen from the table, the raspberry-like SbPt NPs exhibited an excellent electrocatalytic activity. Apparently, the raspberry-like SbPt NPs demonstrated a much better electrochemical performance than intermediate SbPt. This may be because the uneven surface of the raspberry-like structure could provide extensive active sites and further contribute to the enhancement of the catalytic performance [36]. In Fig. S5, the BET measurement is presented. The raspberry-like SbPt NPs exhibited the surface area of 88.20 m^2 g^{-1}, which is much higher than the 1.22 m^2 g^{-1} of theoretical sphere value. The BET values of the raspberry-like SbPt NPs are reasonable and could effectively enhance the surface area compared with the non-porous sphere structures. The HER kinetics were further assessed using the corresponding Tafel slopes (Fig. 5(b)). As presented in Fig. 5(b), intermediate SbPt, Pt black, and raspberry-like SbPt NPs exhibit the values of 59.49, 51.17, and 50.45 mV dec^{-1}, respectively. To investigate the rate determining step in the evolution of H_2, three fundamental mechanisms are considered: Volmer, Heyrovsky, and the Tafel [40,41]. The Volmer mechanism ($H^+ + e^- \rightarrow H_{ad}$) is the first and imperative mechanism which involves the adsorption of proton, and the second mechanism forming H_2 molecule *via* the Heyrovsky mechanism ($H_{ad} + H^+ + e^- \rightarrow H_2$) or Tafel mechanism ($H_{ad} + H_{ad} \rightarrow H_2$). The difference between the Heyrovsky and Tafel mechanisms could be suggested by the Tafel slope, in which from 42 to 118 mV dec^{-1} be the former reaction and from 29 to ~0 (limiting current) mV dec^{-1} be the latter reaction. Hence, by observing the Tafel slopes of the materials, the reaction pathway of the raspberry-like SbPt NPs have the potential to demonstrate the Volmer–Heyrovsky mechanism. Moreover, lower Tafel slopes indicate a higher electrocatalytic activity that is beneficial to HER [42]. In Fig. 5(c), electrochemical impedance spectroscopy (EIS) measurements were performed under an applied voltage of − 0.12 V (*vs.* RHE) in the range from 10^5 to 0.01 Hz, thus confirming that the raspberry-like SbPt NPs exhibited an improved charge transport property than Pt black. As presented in Fig. 5(c), the EIS of HER is composed of three resistances: R_s, R_{ct}, and R_3. R_s indicates the outer solution resistance, which is supposed to be quite similar for the same equipment. R_{ct} indicates the charge transfer resistance. When the first circle

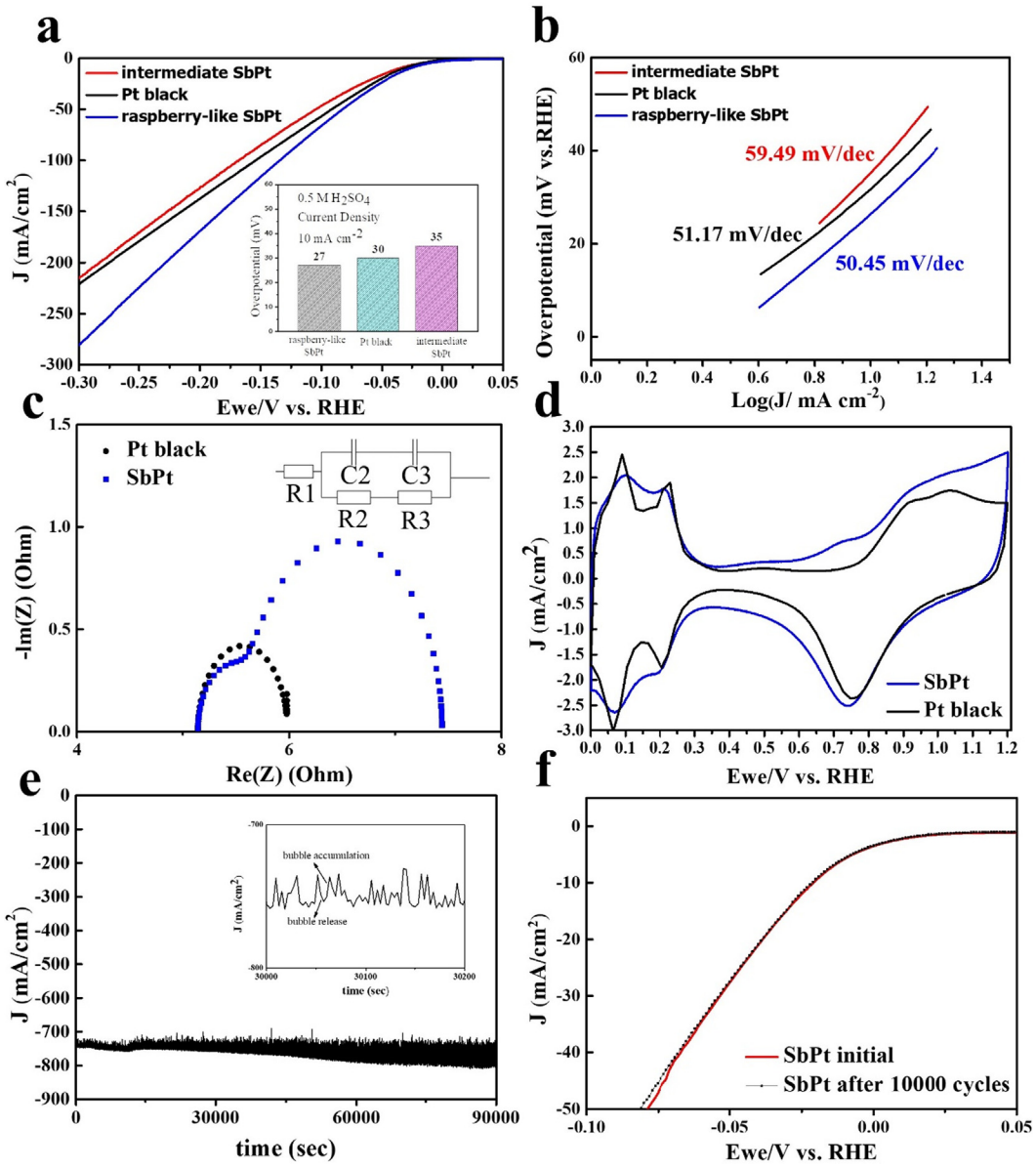

Fig. 5. (a) HER polarization curves for intermediate SbPt, Pt black, and SbPt raspberry-like recorded at 5 mV s^{-1} with inset of corresponding overpotentials at 10 mA cm^{-2}. (b) Corresponding Tafel slopes. (c) Electrochemical impedance spectroscopy (EIS) measurements carried out under −0.12 V (*vs.* RHE) with frequency range of 10^5 to 0.01 Hz. (d) Cyclic voltammograms from 0.0 V to 1.2 V in 0.5 M H_2SO_4. (e) Stability test with applied 0.5 V (*vs.* RHE) over 90,000 s, the inset is the enlargement of the time region from 30,000 to 30,200 s. (f) LSV curves, initial and after 10,000 cycles from 0.1 V to −0.5 V with scan rate 100 mV s^{-1}.

is closer to the Y axis, there is a higher charge transport property; in addition, the first curve of the raspberry-like SbPt NPs is smaller than that of Pt black, indicating a better charge transport property than Pt black. The ECSA of the Pt catalyst can be determined by the adsorption/desorption area of the cyclic voltammogram [43]. In Fig. 5(d), based on the calculation of ECSA = Q/(m*q) [44,45] where q (0.21 mC cm^{-2}) denotes the characteristic adsorption value of the charge density related to the monolayer H_2 atoms on the Pt surface. The calculated ECSA value of the as-prepared raspberry-like SbPt NPs is 33.6 m^2 g^{-1}, which is 1.25 times larger than that of Pt black (Fig. S6). Another key indicator for electrocatalysis is the long-term durability [46,47], which indicates the stability of the activity and the lifespan, thus offering a practical alternative application. Fig. 5(e) presents the measurement of i-t curve under an applied voltage of −0.5 V for 90,000 s. After the stability test, it remained high activity compared with the initial. Moreover, the raspberry-like SbPt NPs exhibited excellent durability (Fig. 5(f)). It remained similar i-t curve without IR compensation after 10,000 cycles under an applied voltage of 0.1 to −0.5 V at a scan rate of 100 mV s^{-1}. Based on the electrochemical evidences previously mentioned, the raspberry-like SbPt NPs exhibited an efficient and sustainable activity in HER. It has been proven that the presence of Sb 3d broadened the Pt surface d-band, which resulted in the drastic improvement of the synergistic effects. The mechanisms inside are suggested to be the Volmer and Heyrovsky mechanisms. The reasons for the excellent catalytic performances can be attributed to the adoption of H* on the SbPt surface. Thus, further DFT simulation should be conducted.

The calculated ΔG_{H^*} has been regarded as the widely accepted descriptor for HER [48,49]. Moreover, the DFT calculations demonstrate that the H adsorption strength of SbPt is weakened by the introduction of Sb to facilitate the H_2 generation surface. In general, an efficient electrocatalyst in HER should exhibit zero ΔG_{H^*} [50–52], thus providing fast proton–electron transfer steps and rapid H_2 release. The DFT results (Figs. 6 and S7–S9) of the observed crystal facets of the raspberry-like SbPt NPs were

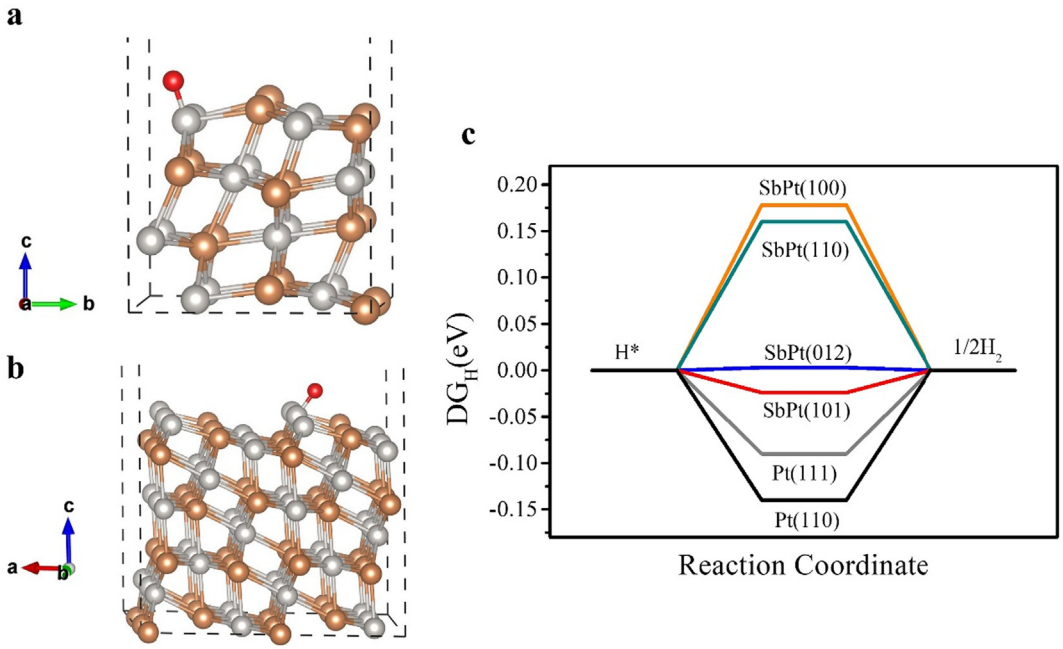

Fig. 6. DFT simulated adsorption sites of H* on the surface of SbPt of (a) (012) and (b) (101). (c) Calculated free energy diagram with different adsorption sites of H* at equilibrium potential for SbPt (100), (110), (012), and (101); Pt (111) and (110).

(110), (100), (101), and (012), exhibiting 0.16, 0.178, −0.024, and 0.003 eV, respectively. The ΔG_{H^*} of Pt crystal planes (111) and (110) were −0.09 and −0.14 eV, respectively [53,54]; the four calculated crystal planes were all active sites with different adsorption energies, Two of these crystal planes, i.e., (012) and (101), exhibited an outstanding performance, which were much closer to zero than those of the classic Pt crystal planes, i.e., (111) and (110). The DFT results revealed that the crystal planes of the raspberry-like SbPt NPs were moderated to construct the HER pathway in the chemisorption of H* generating the superior HER activity. The experimental results were in good agreement with the DFT results. The raspberry-like SbPt NPs exposed accessible (110), (100), (101), and (012) facets, which were observed in both the XRD patterns and SAED measurements. The XRD pattern and EIS curve (Fig. S10) of the raspberry-like SbPt NPs after 90,000 s under an applied voltage of −0.5 V were also provided for durability, and the remaining facets were still correspond to the original XRD diffraction peaks. Furthermore, it has been reported that these crystal facets can be used as highly active electrocatalysts for HER, including CoP [55] with (101), (100), (102), and (110) planes and $Ni_3Sn_2S_2$ [56] quantum dots with (101), (012), and (110) planes. Interestingly, the $Ni_3Sn_2S_2$ quantum dots greatly enhance electrochemical HER over Ni_3S_2, which shows a similar result to the DFT simulation that demonstrates that the (012) surface is the most active site. The existence of 3d orbital hybridization can hinder the adsorption of H and thus provide a highly active site. Based on the evidence discussed previously, the raspberry-like SbPt NPs exhibit higher activity (27 mV to achieve 10 mA cm^{-2}) than Pt, which can be explained by the highly active (110), (100), (101), and (012) planes for HER and the contribution of the unique raspberry-like structure to higher surface area, change in the d-band center shift, and the geometric effect [57].

4. Conclusion

In summary, this work reported the synthesis of new colloidal raspberry-like SbPt NPs, which are applied in the field of HER. The unique raspberry-like structure provides higher surface area for the electrochemical reaction. The calculated ECSA value of the as-prepared raspberry-like SbPt NPs is 33.6 m^2 g^{-1}, which is 1.25 times larger than that of Pt black. Based on the voltage applied to reach the current density of 10 mA cm^{-2}, the overpotential of the raspberry-like SbPt NPs is only 27 mV, with no IR compensation, whereas Pt and intermediate SbPt required 30 and 35 mV. The raspberry-like SbPt NPs exhibited efficient activity and long-term durability in the cycling tests of over 10,000 cycles under an applied voltage of 0.1 to −0.5 V (*vs.* RHE) and long-term durability tests for 90,000 s under an applied voltage of 0.5 V (*vs.* RHE). Furthermore, the DFT results were consistent with the experimental results. The raspberry-like SbPt NPs were found to exhibit highly active (110), (100), (101), and (012) planes. Moreover, the existence of Sb can exert predictable geometric structural and synergistic effects from 3d orbital hybridization can restrain the adsorption of H, and thus to exhibit remarkable electrochemical performance. The synthesis of new colloidal raspberry-like SbPt NPs is essential to elucidate the fundamental properties of the nanomaterial and nanostructure design. In addition, this study could enhance the development of Pt-group materials that can be used as electrocatalysts for HER.

CRediT authorship contribution statement

Chen-Ying Chan: Conceptualization, Methodology, Data curation, Investigation. **Chao-Hung Chang:** Methodology, Data curation. **Hsing-Yu Tuan:** Supervision, Conceptualization, Writing-Reviewing and Editing.

Declaration of Competing Interest

The authors declare that they have no known competing financial interests or personal relationships that could have appeared to influence the work reported in this paper.

Acknowledgements

We acknowledge the financial support by the Ministry of Science and Technology through the grants of MOST 108-2636-E-007-013, MOST 108-2622-8-007-016, and MOST 109-2636-E-007-011 and by National Tsing Hua University through the grant of 107Q2708E1.

Appendix A. Supplementary material

Supplementary data to this article can be found online at https://doi.org/10.1016/j.jcis.2020.09.099.

References

[1] Z. Pu, J. Zhao, I.S. Amiinu, W. Li, M. Wang, D. He, S. Mu, A universal synthesis strategy for P-rich noble metal diphosphide-based electrocatalysts for the hydrogen evolution reaction, Energy Environ. Sci. 12 (3) (2019) 952–957.
[2] Y. Zhao, F. Zhao, X. Wang, C. Xu, Z. Zhang, G. Shi, L. Qu, Graphitic carbon nitride nanoribbons: graphene-assisted formation and synergic function for highly efficient hydrogen evolution, Angew. Chem. Int. Ed. 53 (2014) 13934–13939.
[3] D.Y. Chung, J.M. Yoo, Y.E. Sung, Highly durable and active Pt-based nanoscale design for fuel-cell oxygen-reduction electrocatalysts, Adv. Mater. 30 (2018) 1704123.
[4] C.-Y. Chan, C.-H. Chang, H.-Y. Tuan, Colloidal synthesis of porous red phosphorus nanoparticles as a metal-free electrocatalyst for the hydrogen evolution reaction, Chem. Commun. 56 (19) (2020) 2937–2940.
[5] Y. Li, F. Chu, Y. Liu, Y. Kong, Y. Tao, Y. Li, Y. Qin, An ultrafine ruthenium nanocrystal with extremely high activity for the hydrogen evolution reaction in both acidic and alkaline media, Chem. Commun. 54 (93) (2018) 13076–13079.
[6] Z. Cui, H. Chen, M. Zhao, D. Marshall, Y. Yu, H. Abruña, F.J. DiSalvo, Synthesis of structurally ordered Pt 3 Ti and Pt 3 V nanoparticles as methanol oxidation catalysts, J. Am. Chem. Soc. 136 (29) (2014) 10206–10209.
[7] T. Ghosh, B.M. Leonard, Q. Zhou, F. DiSalvo, Pt alloy and intermetallic phases with V, Cr, Mn, Ni, and Cu: Synthesis as nanomaterials and possible applications as fuel cell catalysts, J. Mater. Chem. 22 (2010) 2190–2202.
[8] S. Guo, S. Sun, FePt nanoparticles assembled on graphene as enhanced catalyst for oxygen reduction reaction, J. Am. Chem. Soc. 134 (5) (2012) 2492–2495.
[9] J. Huang, Y. Song, D. Ma, Y. Zheng, M. Chen, H. Wan, The effect of the support on the surface composition of PtCu alloy nanocatalysts: In situ XPS and HS-LEIS studies, Chin. J. Catal. 38 (7) (2017) 1229–1236.
[10] T. Ishimoto, M. Koyama, Electronic structure and phase stability of PdPt nanoparticles, J. Phys. Chem. Lett. 7 (5) (2016) 736–740.
[11] S.-C. Lim, C.-Y. Chan, K.-T. Chen, H.-Y. Tuan, Synthesis of popcorn-shaped gallium-platinum (GaPt3) nanoparticles as highly efficient and stable electrocatalysts for hydrogen evolution reaction, Electrochim. Acta 297 (2019) 288–296.
[12] S.-C. Lim, M.-C. Hsiao, M.-D. Lu, Y.-L. Tung, H.-Y. Tuan, Synthesis of germanium–platinum nanoparticles as high-performance catalysts for spray-deposited large-area dye-sensitized solar cells (DSSC) and the hydrogen evolution reaction (HER), Nanoscale 10 (35) (2018) 16657–16666.
[13] Z. Qi, C. Xiao, C. Liu, T.W. Goh, L. Zhou, R. Maligal-Ganesh, Y. Pei, X. Li, L.A. Curtiss, W. Huang, Sub-4 nm PtZn intermetallic nanoparticles for enhanced mass and specific activities in catalytic electrooxidation reaction, J. Am. Chem. Soc. 139 (13) (2017) 4762–4768.
[14] E.V. Shevchenko, D.V. Talapin, A.L. Rogach, A. Kornowski, M. Haase, H. Weller, Colloidal synthesis and self-assembly of CoPt 3 nanocrystals, J. Am. Chem. Soc. 124 (38) (2002) 11480–11485.
[15] L. Wu, A.P. Fournier, J.J. Willis, M. Cargnello, C.J. Tassone, In situ X-ray scattering guides the synthesis of uniform PtSn nanocrystals, Nano Lett. 18 (6) (2018) 4053–4057.
[16] T. Xia, J. Liu, S. Wang, C. Wang, Y. Sun, L. Gu, R. Wang, Enhanced catalytic activities of NiPt truncated octahedral nanoparticles toward ethylene glycol oxidation and oxygen reduction in alkaline electrolyte, ACS Appl. Mater. Interfaces 8 (17) (2016) 10841–10849.
[17] J. Greeley, T.F. Jaramillo, J. Bonde, I.b. Chorkendorff, J.K. Nørskov, Computational high-throughput screening of electrocatalytic materials for hydrogen evolution, Nat. Mater. 5 (11) (2006) 909–913.
[18] T. Chao, X. Luo, W. Chen, B. Jiang, J. Ge, Y. Lin, G. Wu, X. Wang, Y. Hu, Z. Zhuang, Y. Wu, X. Hong, Y. Li, Atomically dispersed copper-platinum dual sites alloyed with palladium nanorings catalyze the hydrogen evolution reaction, Angew. Chem. 129 (50) (2017) 16263–16267.
[19] L.u. Li, G. Zhang, B. Wang, T. Yang, S. Yang, Electrochemical formation of PtRu bimetallic nanoparticles for highly efficient and pH-universal hydrogen evolution reaction, J. Mater. Chem. A 8 (4) (2020) 2090–2098.
[20] G. Wang, W. Li, N. Wu, B. Huang, L.i. Xiao, J. Lu, L. Zhuang, Unraveling the composition-activity relationship of Pt Ru binary alloy for hydrogen oxidation reaction in alkaline media, J. Power Sources 412 (2019) 282–286.
[21] J.R. Kitchin, J.K. Nørskov, M.A. Barteau, J. Chen, Role of strain and ligand effects in the modification of the electronic and chemical properties of bimetallic surfaces, Phys. Rev. Lett. 93 (2004) 156801.
[22] H. Yang, J. Zhang, K. Sun, S. Zou, J. Fang, Enhancing by weakening: electrooxidation of methanol on Pt3Co and Pt nanocubes, Angew. Chem. 122 (2010) 7000–7003.
[23] J.R. Kitchin, J.K. Nørskov, M.A. Barteau, J.G. Chen, Modification of the surface electronic and chemical properties of Pt(111) by subsurface 3d transition metals, J. Chem. Phys. 120 (21) (2004) 10240–10246.
[24] M. He, K. Kravchyk, M. Walter, M.V. Kovalenko, Monodisperse antimony nanocrystals for high-rate Li-ion and Na-ion battery anodes: nano versus bulk, Nano Lett. 14 (2014) 1255–1262.
[25] Y.u. Rong, S. Kim, F. Su, D. Myers, M. Taya, New effective process to fabricate fast switching and high contrast electrochromic device based on viologen and Prussian blue/antimony tin oxide nano-composites with dark colored state, Electrochim. Acta 56 (17) (2011) 6230–6236.
[26] J. Liu, Y. Zhang, C. Guo, Thermodynamic assessment of the Pt-Sb system, Int. J. Nonferrous Met. 02 (03) (2013) 95–99.
[27] L. Zhang, D. Xia, Electrocatalytic activity of ordered intermetallic PtSb for methanol electro-oxidation, Appl. Surf. Sci. 252 (6) (2006) 2191–2195.
[28] S. Lee, H.J. Kim, E.J. Lim, Y. Kim, Y. Noh, G.W. Huber, W.B. Kim, Highly selective transformation of glycerol to dihydroxyacetone without using oxidants by a PtSb/C-catalyzed electrooxidation process, Green Chem. 18 (9) (2016) 2877–2887.
[29] M. Rodrigues da Silva, A.C.D. Ângelo, Synthesis and characterization of ordered intermetallic nanostructured PtSn/C and PtSb/C and evaluation as electrodes for alcohol oxidation, Electrocatalysis 1 (2-3) (2010) 95–103.
[30] M. Wakisaka, S. Mitsui, Y. Hirose, K. Kawashima, H. Uchida, M. Watanabe, Electronic structures of Pt−Co and Pt−Ru alloys for CO-tolerant anode catalysts in polymer electrolyte fuel cells studied by EC−XPS, J. Phys. Chem. B 110 (46) (2006) 23489–23496.
[31] A. Darwiche, L. Bodenes, L. Madec, L. Monconduit, H. Martinez, Impact of the salts and solvents on the SEI formation in Sb/Na batteries: An XPS analysis, Electrochim. Acta 207 (2016) 284–292.
[32] D.J. Morgan, Metallic antimony (Sb) by XPS, Surf. Sci. Spectra 24 (2) (2017) 024004.
[33] B.P. Vinayan, S. Ramaprabhu, Platinum–TM (TM = Fe, Co) alloy nanoparticles dispersed nitrogen doped (reduced graphene oxide-multiwalled carbon nanotube) hybrid structure cathode electrocatalysts for high performance PEMFC applications, Nanoscale 5 (11) (2013) 5109–5118.
[34] Y.-C. Shi, J.-J. Feng, X.-X. Lin, L.u. Zhang, J. Yuan, Q.-L. Zhang, A.-J. Wang, One-step hydrothermal synthesis of three-dimensional nitrogen-doped reduced graphene oxide hydrogels anchored PtPd alloyed nanoparticles for ethylene glycol oxidation and hydrogen evolution reactions, Electrochim. Acta 293 (2019) 504–513.
[35] C. Peng, Y. Hu, M. Liu, Y. Zheng, Hollow raspberry-like PdAg alloy nanospheres: High electrocatalytic activity for ethanol oxidation in alkaline media, J. Power Sources 278 (2015) 69–75.
[36] Z. Li, V. Ravaine, S. Ravaine, P. Garrigue, A. Kuhn, Raspberry-like gold microspheres: Preparation and electrochemical characterization, Adv. Funct. Mater. 17 (4) (2007) 618–622.
[37] B. Bai, N. Quici, Z. Li, G.L. Puma, Novel one step fabrication of raspberry-like TiO2@yeast hybrid microspheres via electrostatic-interaction-driven self-assembled heterocoagulation for environmental applications, Chem. Eng. J. 170 (2-3) (2011) 451–456.
[38] Q. Liu, W. Deng, C.-F. Sun, A potassium–tellurium battery, Energy Storage Mater. 28 (2020) 10–16.
[39] M. Zeng, Y. Li, Recent advances in heterogeneous electrocatalysts for the hydrogen evolution reaction, J. Mater. Chem. A 3 (29) (2015) 14942–14962.
[40] Q. Tang, D.-E. Jiang, Mechanism of hydrogen evolution reaction on 1T-MoS_2 from first principles, ACS Catal. 6 (8) (2016) 4953–4961.
[41] J.-Y. Chen, S.-L. Jheng, C.-Y. Chan, H.-Y. Tuan, Morphology controlled synthesis of Pd2Ge nanostructures and their shape-dependent catalytic properties for hydrogen evolution reaction, Int. J. Hydrogen Energy 44 (26) (2019) 12958–12970.
[42] X.Y. Xu, X.F. Dong, Z.J. Bao, R. Wang, J.G. Hu, H.B. Zeng, Three electron channels toward two types of active sites in MoS 2 @Pt nanosheets for hydrogen evolution, J. Mater. Chem. A 5 (43) (2017) 22654–22661.
[43] M. Yang, Q. Cai, C. Liu, R. Wu, D. Sun, Y. Chen, Y. Tang, T. Lu, Monodispersed hollow platinum nanospheres: facile synthesis and their enhanced electrocatalysis for methanol oxidation, J. Mater. Chem. A 2 (2014) 13738–13743.
[44] M. Guo, Q. Tu, L. Wang, Y. Tang, H. Song, J. Zhou, Z. Zhang, Y. Wang, C. Liu, Hollow Pt skim-sandwiched Cu spheres supported on reduced graphene oxide-carbon nanotube architecture for efficient methanol electrooxidation, Int. J. Hydrogen Energy 44 (13) (2019) 6886–6895.
[45] X. Weng, Q. Liu, A.-J. Wang, J. Yuan, J.-J. Feng, Simple one-pot synthesis of solid-core@porous-shell alloyed PtAg nanocrystals for the superior catalytic activity toward hydrogen evolution and glycerol oxidation, J. Colloid Interface Sci. 494 (2017) 15–21.
[46] B.o. Lin, Z. Lin, S. Chen, M. Yu, W. Li, Q. Gao, M. Dong, Q. Shao, S. Wu, T. Ding, Z. Guo, Surface intercalated spherical MoS 2x Se 2(1−x) nanocatalysts for highly efficient and durable hydrogen evolution reactions, Dalton Trans. 48 (23) (2019) 8279–8287.

[47] W. Zhu, C. Tang, D. Liu, J. Wang, A.M. Asiri, X. Sun, A self-standing nanoporous MoP_2 nanosheet array: an advanced pH-universal catalytic electrode for the hydrogen evolution reaction, J. Mater. Chem. A 4 (2016) 7169–7173.
[48] Y. Jiao, Y. Zheng, M. Jaroniec, S.Z. Qiao, Design of electrocatalysts for oxygen- and hydrogen-involving energy conversion reactions, Chem. Soc. Rev. 44 (8) (2015) 2060–2086.
[49] Z. Li, J.-Y. Fu, Y.i. Feng, C.-K. Dong, H. Liu, X.-W. Du, A silver catalyst activated by stacking faults for the hydrogen evolution reaction, Nat. Catal. 2 (12) (2019) 1107–1114.
[50] J.-S. Li, Y. Wang, C.-H. Liu, S.-L. Li, Y.-G. Wang, L.-Z. Dong, Z.-H. Dai, Y.-F. Li, Y.-Q. Lan, Coupled molybdenum carbide and reduced graphene oxide electrocatalysts for efficient hydrogen evolution, Nat. Commun. 7 (2016) 1–8.
[51] Y. Liu, G. Yu, G.-D. Li, Y. Sun, T. Asefa, W. Chen, X. Zou, Coupling Mo_2C with nitrogen-rich nanocarbon leads to efficient hydrogen-evolution electrocatalytic sites, Angew. Chem. 127 (37) (2015) 10902–10907.
[52] T. Liu, P. Li, N. Yao, G. Cheng, S. Chen, W. Luo, Y. Yin, CoP-Doped MOF-based electrocatalyst for pH-universal hydrogen evolution reaction, Angew. Chem. 131 (14) (2019) 4727–4732.
[53] E. Cao, Z. Chen, H. Wu, P. Yu, Y. Wang, F. Xiao, S. Chen, S. Du, Y. Xie, Y. Wu, Z. Ren, Boron-induced electronic-structure reformation of CoP nanoparticles drives enhanced pH-universal hydrogen evolution, Angew. Chem. 132 (10) (2020) 4183–4189.
[54] S. Gudmundsdóttir, E. Skúlason, K.-J. Weststrate, L. Juurlink, H. Jónsson, Hydrogen adsorption and desorption at the Pt(110)-(1×2) surface: experimental and theoretical study, Phys. Chem. Chem. Phys. 15 (17) (2013) 6323.
[55] T. Liu, X. Ma, D. Liu, S. Hao, G. Du, Y. Ma, A.M. Asiri, X. Sun, L. Chen, Mn doping of CoP nanosheets array: an efficient electrocatalyst for hydrogen evolution reaction with enhanced activity at all pH values, ACS Catal. 7 (2017) 98–102.
[56] S.-Y. Lu, S. Li, M. Jin, J. Gao, Y. Zhang, Greatly boosting electrochemical hydrogen evolution reaction over Ni3S2 nanosheets rationally decorated by Ni3Sn2S2 quantum dots, Appl. Catal. B 267 (2020) 118675.
[57] G. Selvarani, S.V. Selvaganesh, S. Krishnamurthy, G.V.M. Kiruthika, P. Sridhar, S. Pitchumani, A.K. Shukla, A methanol-tolerant carbon-supported Pt–Au alloy cathode catalyst for direct methanol fuel cells and its evaluation by DFT, J. Phys. Chem. C 113 (17) (2009) 7461–7468.